

# Direct constraint on the distance of $\gamma^2$ Velorum from AMBER/VLTI observations. \*

F. Millour<sup>1,2</sup>, R. G. Petrov<sup>1</sup>, O. Chesneau<sup>3</sup>, D. Bonneau<sup>3</sup>, L. Dessart<sup>6</sup>, C. Bechet<sup>7</sup>, I. Tallon-Bosc<sup>7</sup>, M. Tallon<sup>7</sup>, E. Thiébaut<sup>7</sup>, F. Vakili<sup>1</sup>, F. Malbet<sup>2</sup>, D. Mourard<sup>3</sup>, G. Zins<sup>2</sup>, A. Roussel<sup>3</sup>, S. Robbe-Dubois<sup>1</sup>, P. Puget<sup>2</sup>, K. Perraut<sup>2</sup>, F. Lisi<sup>4</sup>, E. Le Coarer<sup>2</sup>, S. Lagarde<sup>3</sup>, P. Kern<sup>2</sup>, L. Glück<sup>2</sup>, G. Duvert<sup>2</sup>, A. Chelli<sup>2</sup>, Y. Bresson<sup>3</sup>, U. Beckmann<sup>5</sup>, P. Antonelli<sup>3</sup>, G. Weigelt<sup>5</sup>, N. Ventura<sup>2</sup>, M. Vannier<sup>1,8</sup>, J.-C. Valtier<sup>3</sup>, L. Testi<sup>4</sup>, E. Tatulli<sup>2,4</sup>, D. Tasso<sup>3</sup>, P. Stefanini<sup>4</sup>, P. Stee<sup>3</sup>, W. Solscheid<sup>5</sup>, D. Schertl<sup>5</sup>, P. Salinari<sup>4</sup>, M. Sacchettini<sup>2</sup>, A. Richichi<sup>9</sup>, F. Reynaud<sup>10</sup>, S. Rebattu<sup>3</sup>, Y. Rabbia<sup>3</sup>, T. Preibisch<sup>5</sup>, C. Perrier<sup>2</sup>, F. Pacini<sup>4</sup>, K. Ohnaka<sup>5</sup>, E. Nussbaum<sup>5</sup>, D. Mouillet<sup>2,14</sup>, J.-L. Monin<sup>2</sup>, P. Mège<sup>2</sup>, P. Mathias<sup>3</sup>, G. Martinot-Lagarde<sup>11,15</sup>, G. Mars<sup>3</sup>, A. Marconi<sup>4</sup>, Y. Magnard<sup>2</sup>, B. Lopez<sup>3</sup>, D. Le Contel<sup>3</sup>, J.-M. Le Contel<sup>3</sup>, S. Kraus<sup>5</sup>, D. Kamm<sup>3</sup>, K.-H. Hofmann<sup>5</sup>, O. Hernandez Utrera<sup>2</sup>, M. Heininger<sup>5</sup>, M. Heiden<sup>5</sup>, C. Gil<sup>2</sup>, E. Giani<sup>4</sup>, A. Glentzlin<sup>3</sup>, S. Gennari<sup>4</sup>, A. Gallardo<sup>2</sup>, D. Fraix-Burnet<sup>2</sup>, R. Foy<sup>7</sup>, E. Fossat<sup>1</sup>, T. Forveille<sup>2</sup>, D. Ferruzzi<sup>4</sup>, P. Feautrier<sup>2</sup>, M. Dugué<sup>3</sup>, T. Driebe<sup>5</sup>, A. Domiciano de Souza<sup>1</sup>, A. Delboulbé<sup>2</sup>, C. Connot<sup>5</sup>, J. Colin<sup>3</sup>, J.-M. Clauisse<sup>3</sup>, F. Cassaing<sup>12</sup>, S. Busoni<sup>4</sup>, S. Bonhomme<sup>3</sup>, T. Blöcker<sup>5</sup>, J. Behrend<sup>5</sup>, C. Baffa<sup>4</sup>, E. Aristidi<sup>1</sup>, B. Arezki<sup>2</sup>, K. Agabi<sup>1</sup>, B. Acke<sup>2,13</sup>, M. Accardo<sup>4</sup>, M. Kiekebusch<sup>8</sup>, F. Rantakyrö<sup>8</sup>, and M. Schöller<sup>8</sup>

(Affiliations can be found after the references)

Received; accepted

## ABSTRACT

**Context.** Interferometry can provide spatially *resolved* observations of massive star binary systems and their colliding winds, which thus far have been studied mostly by means of spatially *unresolved* observations.

**Aims.** In this work, we present the first AMBER/VLTI observations, taken at orbital phase 0.32, of the Wolf-Rayet and O (WR+O) star binary system  $\gamma^2$  Velorum and use the interferometric observables to constrain its properties.

**Methods.** The AMBER/VLTI instrument was used with the telescopes UT2, UT3, and UT4 on baselines ranging from 46 m to 85 m. It delivered spectrally dispersed visibilities, as well as differential and closure phases, with a resolution  $R = 1500$  in the spectral band 1.95–2.17  $\mu$ m. We interpret these data in the context of a binary system with unresolved components, neglecting in a first approximation the wind-wind collision zone flux contribution.

**Results.** Using WR- and O-star synthetic spectra, we show that the AMBER/VLTI observables result primarily from the contribution of the individual components of the WR+O binary system. We discuss several interpretations of the residuals, and speculate on the detection of an additional continuum component, originating from the free-free emission associated with the wind-wind collision zone (WWCZ), and contributing at most to the observed  $K$ -band flux at the 5% level. Based on the accurate spectroscopic orbit and the Hipparcos distance, the expected absolute separation and position angle at the time of observations were  $5.1 \pm 0.9$  mas and  $66 \pm 15^\circ$ , respectively. However, using theoretical estimates for the spatial extent of both continuum and line emission from each component, we infer a separation of  $3.62_{-0.30}^{+0.11}$  mas and a position angle of  $73_{-11}^{+9} {}^\circ$ , compatible with the expected one. Our analysis thus implies that the binary system lies at a distance of  $368_{-13}^{+38}$  pc, in agreement with recent spectrophotometric estimates, but significantly larger than the Hipparcos value of  $258_{-31}^{+41}$  pc.

**Key words.** Techniques: interferometric – stars: individual:  $\gamma^2$  Velorum - stars: winds, outflows - stars: Wolf-Rayet stars: binaries: spectroscopic - stars: early-type

## 1. Introduction

Send offprint requests to: F. Millour  
e-mail: [Florentin.Millour@unice.fr](mailto:Florentin.Millour@unice.fr)

\* Based on observations made with the Very Large Telescope Interferometer at Paranal Observatory

$\gamma^2$  Velorum constitutes an excellent laboratory for the study of massive stars and their radiatively-driven winds. Indeed,  $\gamma^2$  Velorum (WR 11, HD 68273) is the clos-

est known Wolf-Rayet (WR) star, at a Hipparcos-determined distance of  $258_{-31}^{+41}$  pc (Van der Hucht et al. 1997; Schaerer et al. 1997), whereas other WR objects lie at  $\sim 1$  kpc or beyond. Moreover,  $\gamma^2$  Velorum is an SB2 spectroscopic binary WR+O system (WC8+O7.5III,  $P = 78.53$  d, Schmutz et al. 1997; De Marco & Schmutz 1999) offering access to fundamental parameters of the WR star, usually obtained indirectly through the study of its dense and fast wind. Using spectroscopic modeling of the integrated, but spectrally-dispersed, light from the system, De Marco & Schmutz (1999) and De Marco et al. (2000) provided the most up-to-date fundamental parameters of the individual components of the binary system.

Since  $\gamma^2$  Velorum is relatively bright and well observable at any wavelength, it has been extensively studied by various techniques. In that context,  $\gamma^2$  Velorum represents an unique opportunity to spatially resolve a WR wind by means of optical interferometry. This object was observed by the Narrabri intensity interferometer operating around  $0.45\,\mu\text{m}$  as early as 1968 (Hanbury Brown et al. 1970). By observing such a star with a long baseline interferometer, one may constrain various parameters, such as the binary orbit, the brightness ratio of the two components, the angular size associated with both the continuum and the lines emitted by the WR star.

The collision between the fast and dense wind from the WR and the less dense but faster wind from the O star generates a wealth of phenomena. International Ultraviolet Explorer (IUE) and Copernicus ultraviolet spectra (St.-Louis et al. 1993, and references therein) revealed a variability in UV P-Cygni line profiles, associated with selective line eclipses of the O star light by the WR star wind as well as the carving of the WR wind by the O-star wind (compared to its spherical distribution in the absence of a companion). Air-borne X-ray observation campaigns have revealed additional and invaluable information on the wind-wind collision zone (hereafter WWCZ) (see references in Van der Hucht 2002; Willis et al. 1995; Skinner et al. 2001; Pittard & Stevens 2002; Corcoran et al. 2003; Schild et al. 2004; Henley et al. 2005).

The WR component of the  $\gamma^2$  Velorum system is of a WC8 type. While 50% of such WR stars (and 90% of the WC9 type) show heated ( $T_d \sim 1300\,\text{K}$ ) circumstellar amorphous carbon dust, ISO observations of  $\gamma^2$  Velorum revealed no such dust signatures (Van der Hucht et al. 1997). Keck observations resolved, although only barely, the system in the  $K$  band and confirmed the absence of any dust emission from this system (Monnier et al. 2002), suggesting that if dust is created near the WWCZ, it is in small amounts.

The present paper aims at constraining further our knowledge of the  $\gamma^2$  Velorum system, using long-baseline interferometric observations conducted in near-IR by the VLTI with the newly commissioned instrument AMBER. The results discussed in this paper are limited to observations recorded with a single triplet of baselines in  $K$  band with the AMBER. We concentrate our efforts in pre-

senting the potential of AMBER observations and their complementarity with techniques lacking spatial resolution for the study of massive close binaries. In this context, we perform an in-depth checking of the consistency of the AMBER/VLTI data recorded, with the up-to-date knowledge we have on this well studied binary system.

The paper is organized as follows. In Sect. 2, we describe the AMBER/VLTI observations and the data. In Sect. 3, we present the AMBER data and constrain the system characteristics. The system's parameters are used to predict a basic signal inferred from the knowledge of the spectroscopic orbit, some estimate of the angular diameter of each component, and results from the spectroscopic modeling of the individual stars. We also discuss the potential effects stemming from the WWCZ and their influence on the observed interferometric signal. In Sect. 4, we fit the AMBER observations by concentrating on a few parameters that can be directly constrained, i.e., the angular separation of the components, the orientation of the system projected onto the sky, and the brightness ratio between the two components. We then discuss in Sect. 5 the adequacy of our modeling in reproducing the observations, and present our conclusions in Sect. 6.

## 2. AMBER Observations and data

### 2.1. Observations

AMBER (Astronomical Multi BEam Recombiner) is the VLTI (Very Large Telescope Interferometer) beam combiner operating in the near-infrared (Petrov et al. 2003). The instrument uses spatial filtering with fibers (Mege et al. 2000). The interferometric beam passes through an anamorphic optics compressing the beam perpendicularly to the fringe coding in order to be injected into the slit of a spectrograph. The instrument can operate at spectral resolutions up to 10,000, and efficiently deliver spectrally dispersed visibilities.

$\gamma^2$  Velorum was observed on 25 Dec 2004 during the first night of the first Guaranteed Time Observations (GTO) run of the AMBER instrument on the three projected baselines UT2-UT3 (46m,  $20^\circ$ ), UT3-UT4 (53m,  $84^\circ$ ) and UT2-UT4 (85m,  $55^\circ$ ) of the VLTI (see Fig. 1, left). The Julian day of observation was JD=2,453,365.16.

The AMBER observations have been conducted with a frame exposure time of 60 ms in three spectral windows in the MR-K spectral mode (spectral resolution of 1500,  $K$  band), i.e.,  $1.98\text{--}2.02\,\mu\text{m}$ ,  $2.03\text{--}2.11\,\mu\text{m}$ , and  $2.10\text{--}2.17\,\mu\text{m}$  at hour angle -134 min, -114 min, and -102 min, respectively (left panel of Fig. 1).

HD75063 (spectral type A1III) was observed with the same exposure time and the same spectral windows in order to calibrate the visibilities. Its diameter is estimated to be 0.50 mas with an error of 0.08 mas, using several color indices. This corresponds to a visibility of  $0.988 \pm 0.004$  for the longest base (85m), so that the error on the calibrator

**Table 1.** Log of the observations and atmospheric conditions for  $\gamma^2$  Velorum (top-three rows) and the spectrophotometric calibrator star HD 75063 (bottom-three rows), observed on 25/12/2004.

Time	Star	<i>K</i> Mag.	$\Delta\lambda$	Seeing	Coherence Time	Air Mass
4h18	$\gamma^2$ Velorum	2.1	1.95 - 2.03 $\mu\text{m}$	0.72 ''	4.5 ms	1.213
4h35	$\gamma^2$ Velorum	2.1	2.02 - 2.10 $\mu\text{m}$	0.60 ''	5.3 ms	1.180
4h49	$\gamma^2$ Velorum	2.1	2.09 - 2.17 $\mu\text{m}$	0.73 ''	4.4 ms	1.158
5h57	HD 75063	3.6	1.95 - 2.03 $\mu\text{m}$	0.90 ''	3.6 ms	1.107
6h09	HD 75063	3.6	2.02 - 2.10 $\mu\text{m}$	0.72 ''	4.0 ms	1.097
6h18	HD 75063	3.6	2.09 - 2.17 $\mu\text{m}$	0.58 ''	5.5 ms	1.090

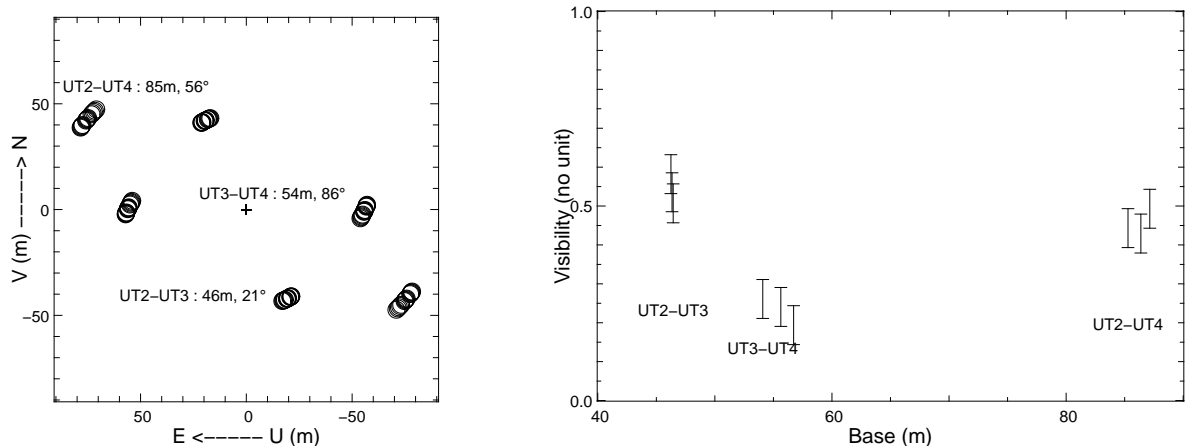


**Fig. 1.** *Left:* Projected baselines showing the range of position angles and base lengths on the sky during the observations. *Right:* Absolute calibrated visibility of  $\gamma^2$  Velorum in function of base length. The strong variations correspond mainly to the partial resolution of the binary star.

diameter translates into a global error on the absolute visibility of less than 1%.

## 2.2. Observing context

The observations of  $\gamma^2$  Velorum were carried out under non optimal conditions as the VLTI + AMBER system was still not in a fully operational state at the moment of the observations. As explained in Malbet et al. (2005), a detailed analysis of the commissioning data has shown that the optical trains of the UT telescopes are affected by non-stationary high-amplitude vibrations. These vibrations affect the continuum visibilities, requiring a careful data processing and calibration procedure. We stress that these vibrations bias the instantaneous estimated visibility but do not affect the closure phase and, since the observed spectral windows are small, the differential estimators.

During these observations, problems were encountered with the UT2 Adaptive Optics associated with difficulties to close the loop and with injections in the fibers. We thus expect calibration problems on the data related to the baselines containing the UT2 telescope. Again, these problems are limited to the absolute visibilities.

The time lag between the observations of the calibrator and the science object is of the order of one hour.

We checked that the atmospheric conditions changed only slightly between the two measurements.

### 2.2.1. Data set

The AMBER/VLTI instrument data processing principles are well described in the articles of Tatulli et al. (2006); Millour et al. (2004). In the current situation, the AMBER/VLTI instrument has a series of issues about data that obliged us to develop a specific data reduction strategy which is fully described in appendices.

The set of data provided by the AMBER instrument (limited to the spectral window 1.95 to 2.17  $\mu\text{m}$ ) is the following:

1. One normalized spectrum (mean spectrum from the three observing telescopes).
2. Three absolute visibilities per observation, providing some information on the projected equivalent size of the object for each baseline.
3. Three differential visibilities curves, providing some information on variation of the projected equivalent size of the object versus wavelength for each baseline.
4. Three differential phase curves, providing some information on the object photocenter relatively to a large continuum reference for each baseline.

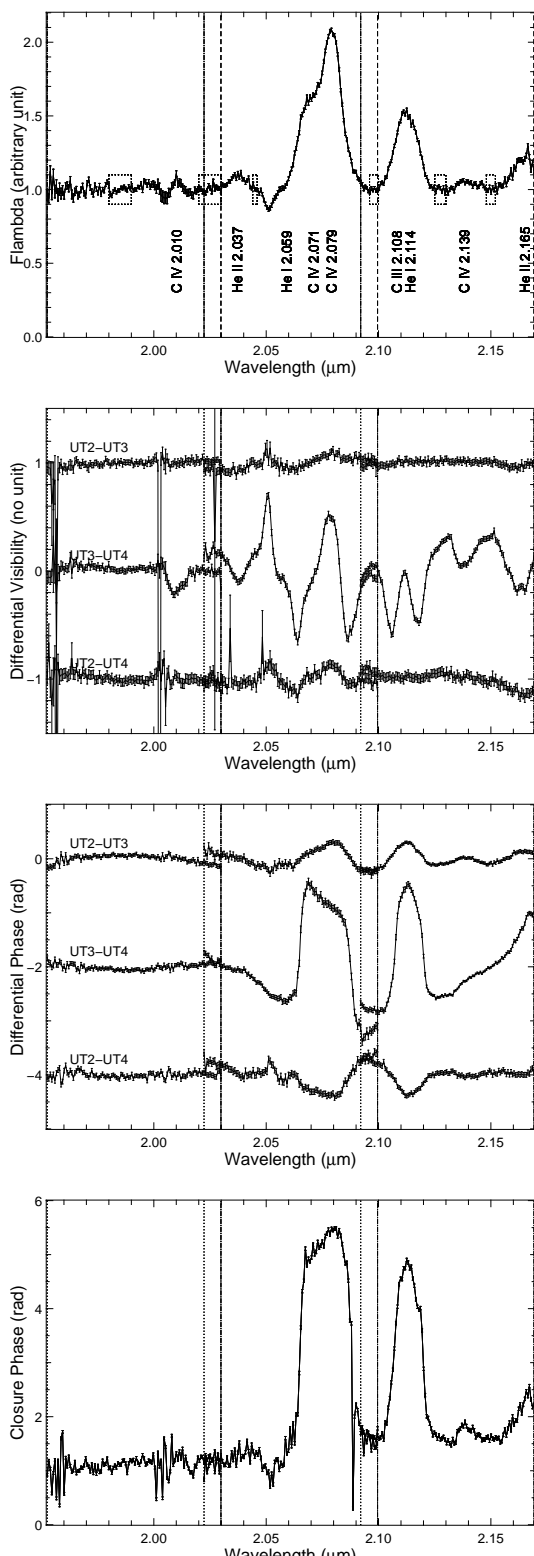


**Fig. 2.** *Top:* Result of the complete spectral calibration, showing the principal lines present in the observed spectrum. The dotted boxes show the selected continuum zones used to redress the observed spectrum. *The other plots from top to bottom:* Observed data with AMBER. You can find respectively the differential visibilities, the differential phases and the closure phase versus wavelength. The differential visibility and differential phase curves from each baselines are arbitrarily shifted for clarity.

5. One closure phase providing some information on the degree of asymmetry of the system's flux distribution computed for a baseline triplet.

The calibrated data are shown in Fig. 1 and Fig. 2. The differential visibilities, differential phase and closure phase show strong variations with wavelength, well beyond the error bars, demonstrating that the  $\gamma^2$  Velorum system has been resolved by the AMBER/VLTI instrument.

The global slope on the closure phase is mainly due to the wavelength dependence of spatial frequencies (pure geometrical effect) whereas the rapid variations in differential visibilities, differential phases and closure phase are due to variations of the flux ratio between the two stars (pure spectroscopic effect). On the contrary, the slope on the differential phases does not have any physical significance since it depends only on the definition of the reference channel.

Note that observations in each spectral window were scanned sequentially, at a quarter-of-an-hour interval. This time lag must be taken into account since we expect the binary signal to be rapidly evolving as the triplet of projected baselines slowly changes due to the earth rotation.

### 3. Stars models based on spectroscopic data

Below, we present the current knowledge of the system, and use its geometrical parameters to estimate the basic signal from this binary system. As a first approach, we neglect any additional emission from dust; we also neglect the free-free emission expected to arise from the WWCZ region. This late assumption is probably less valid physically since the existence of this WWCZ is proved observationnaly<sup>1</sup>.

#### 3.1. Geometrical parameters of the system

The spectroscopic orbit is well determined by Schmutz et al. (1997). The interferometer is sensitive to other geometrical parameters much less constrained, namely the angular separation and angle of position in the sky.

The observations of Hanbury Brown et al. (1970) provided an angular semi-major axis of the orbit of  $4.3 \pm 0.5$  mas, and an angular size for the largest component of  $0.44 \pm 0.05$  mas ( $17 \pm 4 R_\odot$  at a distance estimated to be  $350 \pm 50$  pc).

The orbital parameters are shown in Table 2. They are extracted from the spectroscopic and spectrophotometric observations in Schmutz et al. (1997), De Marco & Schmutz (1999). The inclination derived by De Marco et al. (2000) of  $63 \pm 3$  degree based on the refinement of their model (O and WR V magnitude) is not taken

<sup>1</sup> The WWCZ is characterized by a very hot and dense layer of material at the interface between the two winds (well above the local WR- or O-star wind density) that should contribute significantly to the free-free continuum.

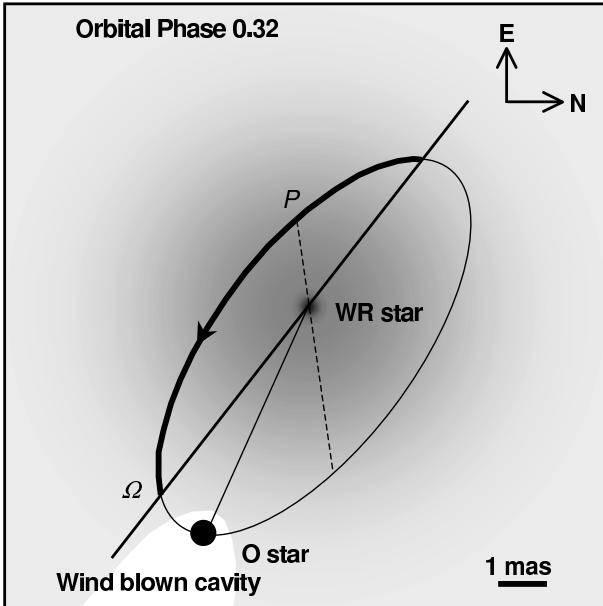


**Fig. 3.** Projection of the true orbit as defined by the spectroscopic parameters (Schmutz et al. 1997) onto the plane of the sky. Note that there is an ambiguity of  $180^\circ$  on the true direction of the WR versus the O star which can be checked over by our interferometric observations.

into account in this study because the error bar is probably underestimated and relies on the Hipparcos distance that may not be correct. Schmutz et al. (1997) performed a new fit of the polarisation data of St.-Louis et al. (1987) but the uncertainty for their  $\Omega$  parameter is not given in the paper. We adopt the standard deviation ( $\pm 11^\circ$ ) of the position angle of the linear polarization vector provided in St.-Louis et al. (1987). Note that this large error may be partially explained by intrinsic variations of the polarization due to the wind-wind collision (see for instance Villar-Sbaffi et al. 2005). We also stress that the angle  $\Omega$  in the polarimetric model of Brown et al. (1982), used in St.-Louis et al. (1987) and Schmutz et al. (1997) denotes the angle between the North and the projection of the rotation axis (orbit normal) on the plane of the sky. This definition do not coincide with the usual definition of the  $\Omega$  parameter used to denote the line of node of binary orbits, but is flipped by  $90^\circ$ .

The combination of the projected orbital radius  $a \sin i$  with the inclination and the distance yields the angular semi-major axis of the relative orbit  $a = 4.8 \pm 0.7$  mas.

We used the Schmutz et al. (1997) ephemeris for  $\gamma^2$  Velorum to calculate the orbital phase at which the observations were performed (see table 2). From the time of periastron passage  $T_0=2,450,119.1$  (HJD), and orbital period  $P=78.53$  days, the periastron occurs at zero phase, the O-type component is in front shortly afterwards at phase  $\Phi = 0.03$  and the WR is in front at phase  $\Phi = 0.61$ . For the date of the VLTI observation ( $T=2,453,365.16$  (HJD)), using this ephemeris and the adopted orbital elements, we find an orbital phase  $\Phi = 0.32 \pm 0.03$ , i.e.,

close to quadrature, and we determine the relative position of the components on the sky. The angular separation of the stars should be  $5.1 \pm 0.9$  mas with a position angle of  $66 \pm 15^\circ$ .

This separation is close to the fringe spacing provided by the baselines. Hence we do not expect to see a fast modulation of the visibility through the wavelength range considered. Nevertheless, the visibility signal changes rapidly between the three different projected baselines of the triplet and as the projected baselines move with the earth rotation.

**Table 2.** Parameters of the system from the studies of Schmutz et al. (1997).

Parameter	Value	Error
Distance	258 pc	+41/-31
Period	78.53 day	0.01
Periastron	2450120.5 day	2
Eccentricity	0.326	0.01
Periastron longitude $\omega_{WR}$	$68^\circ$	4
$a_1 \sin i$	$39.10^6$ km	$2.10^6$
$a_2 \sin i$	$125.10^6$ km	$2.10^6$
inclination $i$	$65^\circ$	8
PA of node $\Omega$	$232^\circ$	11
$R_O$	$12.4 R_\odot$	1.7
$R_c$ of WR star	$3.0 R_\odot$	0.5
$\theta_O$	0.48 mas	0.09
$\theta_c$ of WR star	0.11 mas	0.06
$\theta_{(\tau_K=1)}$ of WR star	0.28 mas	0.1
$\pi_{(a_1+a_2)}$	4.8 mas	0.7

### 3.2. A model for the individual spectra

Short of performing the full radiation-hydrodynamics problem for the  $\gamma^2$  Velorum system, including the radiation field and force stemming from each stellar component, the optical-depth effects caused by their winds, and the emission from the hot collision zone separating them, we limit ourselves, in this section, to the detailed modeling of the WR and O star fluxes, with the aim of simulating the interferometric signals from these two sources alone.

The model atmosphere computations are carried out with the code CMFGEN (Hillier & Miller 1998), originally designed to model the expanding outflows of WR stars. CMFGEN solves the radiative transfer equation in the comoving frame, under the constraint of radiative and statistical equilibrium, assuming spherical symmetry and a steady state, and is capable of handling line and continuum formation, both in regions of small and high velocities (compared to the thermal velocity of ions and electrons). Hence, it can solve the radiative transfer problem both for O stars, in which the formation regions for lines and continuum extend from the hydrostatic layers out to the

supersonic regions of the wind, and for WR stars where line and continuum both emerge from regions of the wind that may have reached half its asymptotic velocity.

The  $\gamma^2$  Velorum system has been studied in detail by De Marco & Schmutz (1999) and De Marco et al. (2000). For the WR component, we start from a model for WR 135 (Dessart et al. 2000) and adjust the parameters to those of de De Marco et al. (2000). Our WR model parameters are:  $L_* = 10^5 L_\odot$ ,  $\dot{M} = 10^{-5} M_\odot \text{ yr}^{-1}$ , a volume filling factor of 10% that introduces a clumping of the wind at velocities above  $\sim 100 \text{ km s}^{-1}$ ,  $\text{C/He} = 0.15$ , and  $\text{O/He} = 0.03$  (abundances are given by number). The velocity law adopted allows a two-stage acceleration, first a fast acceleration up to a velocity  $v_{\text{ext}} = 1100 \text{ km s}^{-1}$  (characterized by a velocity exponent  $\beta_1 = 1$ ) and a more extended slow acceleration at larger radii (velocities) up to the asymptotic velocity of  $v_\infty = 1550 \text{ km s}^{-1}$  ( $\beta_2 = 20$ ; see Hillier & Miller (1998) for details and their eq. (8) for the velocity law). We associate the stellar surface with the layer where the Rosseland optical depth is  $\sim 20$ . While De Marco et al. (2000) obtained  $T_* = 57 \text{ kK}$  (and  $R_* = 3.2 R_\odot$ ), we find that the near-IR range can be better fitted by adopting a slightly hotter stellar temperature, i.e.,  $T_* = 70 \text{ kK}$  (and  $R_* = 2.2 R_\odot$ ). The higher-temperature model leads to a better match of the near-IR CIV/CIII features, while leaving the optical range still well fitted – only the HeII 4686Å, the CIII 5696Å, and the CIV 5808Å are noticeably affected but still satisfactorily fitted. The general appearance of CIV and CIII in the AMBER spectra is somewhat smoother than in the model, but the absorption at  $2.05 \mu\text{m}$  is perfectly fitted. We note that a line is observed at  $2.138 \mu\text{m}$  not taken into account in our WR model. This line is not an artifact since it is also detected in the visibilities and phases. We employ both models for the interferometric study described below.

For the O-star model (computed with CMFGEN, see Martins et al. (2005)), we select an O8.5 III spectral type (De Marco & Schmutz 1999) and adopt the spectral distribution from Martins et al. (2005)<sup>2</sup>. The corresponding O-star parameters are  $L_* = 1.8 \times 10^5 L_\odot$ ,  $\dot{M} = 4 \times 10^{-7} M_\odot \text{ yr}^{-1}$ ,  $v_\infty = 2240 \text{ km s}^{-1}$ ,  $\log g = 3.6$ , and  $T_* = 32.5 \text{ kK}$ . Other models of O stars were also tested providing some input on the sensitivity of the AMBER data to the O star spectral type.

In our analysis below, we scale both spectra using the  $\gamma^2$  Velorum Hipparcos distance of 258pc, and convolve them with the AMBER instrumental function to provide a spectral resolution of  $\sim 1500$ . Moreover, the very low reddening to the  $\gamma^2$  Velorum system (Van der Hucht et al. 1996) leads to no noticeable extinction in the near-IR and is thus neglected. Following De Marco et al. (2000), we expect a flux ratio between the WR and the O star of 0.8–1 in the near-IR spectral region covered by AMBER. This “free” parameter can also be inferred from our AMBER observations.

<sup>2</sup> A database of O-star spectra is available at <http://www.mpe.mpg.de/~martins/SED.html>

**Table 3.** Line and continuum formation regions corresponding to the WR 11 model, limited to the near-IR range. For each line, we give the radius of the peak emission (in  $R_* = 3 R_\odot$ ) and that of the maximum flux in the line, normalized to the continuum (in brackets). The apparent diameters are scaled to a distance of 258 pc.

Parameter	Radius in $R_*$	UD (mas)
$R_{\tau(2.0\mu\text{m})}$	2.7	0.30
$R_{\tau(2.5\mu\text{m})}$	3.3	0.37
CIV (2.07 $\mu\text{m}$ )	3-7 (2.5)	0.46
CIII/HeI (2.11 $\mu\text{m}$ )	5-10 (1.4)	0.57
HeII/HeI (2.17 $\mu\text{m}$ )	4 (1.2)	0.34
HeII (2.19 $\mu\text{m}$ )	4 (1.3)	0.35

WR outflows are optically thick up to a few stellar radii above the hydrostatic surface. The denser the wind, the larger the radius of the effective photosphere where photons escape, and the more so at longer wavelengths due to the increase in free-free opacity. Table 3 lists the radius where the inward integrated continuum optical depth reaches unity for a range of near-IR wavelength (comparable for both WR models): for a core radius of  $\sim 3 R_\odot$ , this extends from  $1.8$  to  $3.3 R_*$ , from  $1$  to  $2.5 \mu\text{m}$ , equivalent to  $\sim 0.27 \text{ mas}$ . We adopted the Hipparcos distance bearing in mind that the uncertainty on the star radii can be important as a consequence of the distance one (see discussion).

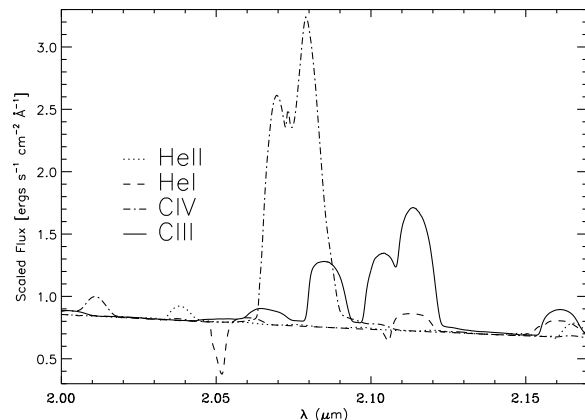


**Fig. 4.** Near-IR synthetic spectra computed by accounting for bound-bound transition of selected ions (HeI: dashed line; HeII: dotted line; CIII: solid lines; CIV: dash-dotted line), illustrating the different line contributions and overlap in the AMBER spectral windows.

Photons falling in spectral regions where they experience line as well as continuum opacity will escape at still larger radii than photons experiencing exclusively continuum opacity.

More generally, in the  $2-2.2 \mu\text{m}$  region, the CIII/CIV/HeII lines form over a region exterior to the (local) continuum photosphere that extends out

only to about a factor of two in radius, corresponding to an angular size of  $\lesssim 0.7$  mas (see table 3). In the  $K$  band, stars with angular diameter below 1 mas are only marginally resolved with a baseline of 100 m. Thus, the variations in WR diameter quoted here are a second-order signal ( $\Delta V \leq 2\%$ ) difficult to extract with the current performances of AMBER instrument. Observations with longer baselines are therefore needed to investigate this particular point<sup>3</sup>.

Assuming a flux ratio of about unity in the continuum and that the two components are essentially unresolved by AMBER, we expect a contrast of unity for the binary modulation (we also assume in this case the absence of other contributions in  $K$  band from dust and/or the WWCZ). Thus, given the slowly changing *continuum* flux ratio between the WR- and O-star components, the presence of lines is expected to lead to a sudden change of the AMBER interferometric signal.

## 4. Analysis of the interferometric data

### 4.1. Analytical fit using visibilities and closure phase

The aim of this section is to infer the geometrical parameters of the binary using absolute interferometric observables exclusively. Specifically, we seek the separation  $\rho$ , the position angle  $\theta$  of the system, and the flux ratio  $R$  between the two components. We perform the fit in the continuum regions defined in Fig. 2.

#### 4.1.1. Method and results

The geometrical model used to fit the data is a standard binary model characterized by the astrometric parameters (position angle, separation, used in the vector  $\vec{\rho}$ ) and the flux ratio between the two stars, i.e.,  $R(\lambda)$ , at a given spatial frequency  $\vec{u}_{jk}$  (see Eq. 1),

$$C_{jk}(\lambda) = \frac{1 + R(\lambda)e^{-2i\pi\vec{u}_{jk} \cdot \vec{\rho}}}{1 + R(\lambda)}. \quad (1)$$

We use this complex visibility to compute the differential visibility and phase. Note that at this stage, the algorithm does not allow to disentangle the irrespective O- and WR-star fluxes. The absolute visibility is  $V_{jk}(\lambda) = |C_{jk}(\lambda)|$ , and the closure phase is  $\psi_{123}(\lambda) = \arctan[C_{12}(\lambda)C_{23}(\lambda)C_{13}^*(\lambda)]$ .

We used the following set of observables to perform the fit:

- The absolute visibility for each selected wavelength.
- The closure phase for each selected wavelength.

The binary parameters obtained with this method are shown in the table. 4. The resulting separation is

<sup>3</sup> Note that the model also account for the large angular diameter found by Hanbury Brown et al. (1970) in the line CIII 0.46  $\mu$ m. Its formation region is one of the most extended of all optical and near-IR lines.

$3.65 \pm 0.12$  mas. The error bar is computed as follows: we have a standard deviation between all the measurements of 0.06 mas, and we have an average estimate by the  $\chi^2$  of the fit to 0.1 mas. Hence the error is on the order of  $\pm 0.12$  mas. The position angle is  $73 \pm 13^\circ$ , and the flux ratio between the two stars is  $0.62 \pm 0.11$ .

#### 4.1.2. Interpretation

The main point is that the obtained separation is not in a good agreement with the expected one  $5.1 \pm 0.9$  mas. On the other hand, the expected position angle of  $66 \pm 15^\circ$  is compatible within the error bars with the measured one. This result is tested in the following sections and discussed in Sect. 5.

We can notice a correlation between the flux ratio and the wavelength. Such a correlation could be explained if the O star is the primary and the WR star is the secondary. However, the estimated flux ratio variation with wavelength is too strong to be explained by this way. Considering the error bars we have, we can only say that this trend is fortuitous and that the flux ratio may be constant over the spectral bandwidth.

We point out to the reader the fact that the flux ratio given by this method is *within* the WR star continuum zones shown in Fig. 2, which means that the average flux ratio on all the bandwidth is slightly different. It corresponds in fact to  $0.79 \pm 0.12$  in average on the 1.95-2.17  $\mu$ m range.

The quality of the fit is not good, the fitted visibilities and closure phase are on average at  $2\sigma$  over the observed ones. This overestimate of visibilities means that the “real” observed object is more resolved than a binary star alone.

The easiest way to improve the fit is to consider a third component for the flux that would be fully spatially resolved and would dilute the correlated flux observed by AMBER. According to the visibilities, this contribution could contribute up to 20% of the overall flux of the system. However, this significant flux would have been detected by other techniques and is not reported in the literature. This may also mean that the observed absolute visibilities on both the UT2-UT3 and UT2-UT4 bases are significantly biased. This may be related to the observation problems we noticed on UT2.

### 4.2. Fit using WR and O stars modeled spectra

In this section we use the synthetic spectra presented in Sect. 3.2 in order to find the parameters that best match our data. We still assume the individual components of the binary system are unresolved.

#### 4.2.1. Method and results

In Sect. 4.1, we restricted the fitting process to a selection of a few narrow continuum windows. We now wish

**Table 4.** Selected continuum zones as in Fig. 2 and the adjustment of the binary star model. It shows globally a constant separation and position angle of 3.65 mas and  $72.7^\circ$ . We have redundant measures separated by 15mn in time at  $2.025\,\mu\text{m}$  and  $2.098\,\mu\text{m}$  since the spectral windows overlapped at this continuum zone. The RMS column corresponds to the standard deviation between all the measurements whereas the  $\Delta$  one represents the average error on the parameters from the fitting process.

Wavelength ( $\mu\text{m}$ )	1.985	2.025 <sub>1</sub>	2.025 <sub>2</sub>	2.045	2.098 <sub>1</sub>	2.098 <sub>2</sub>	2.1275	2.150	Avg.	RMS	$\Delta$
Observation											
Visibility UT2-UT3	0.50	0.52	0.47	0.54	0.54	0.58	0.59	0.59			
Visibility UT3-UT4	0.26	0.26	0.28	0.28	0.23	0.20	0.24	0.26			
Visibility UT2-UT4	0.44	0.43	0.42	0.42	0.41	0.53	0.52	0.48			
Closure Phase	1.09	1.22	1.11	1.37	1.49	1.61	1.78	1.60			
Fit Binary											
Separation (mas)	3.69	3.68	3.57	3.53	3.60	3.72	3.69	3.68	3.65	0.06	0.1
Position Angle ( $^\circ$ )	64.0	64.8	93.4	68.8	76.4	72.3	71.1	70.8	72.7	8.7	10
Flux Ratio 2nd star	0.57	0.57	0.57	0.59	0.64	0.68	0.66	0.64	0.62	0.04	0.1

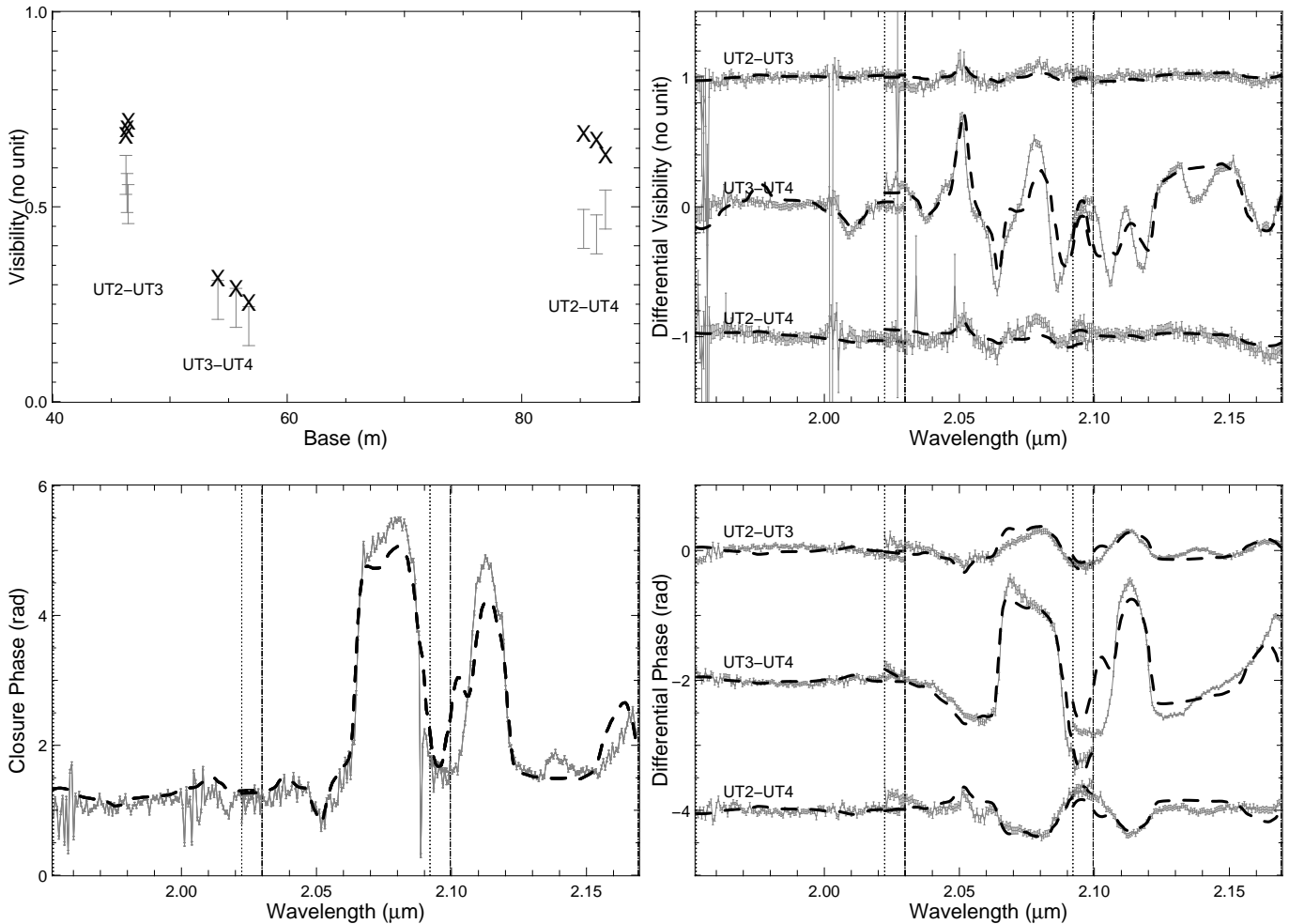


**Fig. 5.** Observed data with AMBER and the best fit, using a geometrical model of a double star and a O- and WR-star synthetic spectra of Sect. 4.2. *top-left*: Points with error bars: observed absolute visibilities versus base length. Crosses: our model. See text for comments. *top-right*: Gray line with error bars: observed differential visibilities versus wavelength. Dashed line: our model. The different baselines are offset for clarity. *bottom-left*: Gray line with error bars: observed closure phase versus wavelength. Dashed line: the model. See text for comments. *bottom-right*: Gray line with error bars: observed differential phases versus wavelength. Dashed line: our model. The different baselines are offset for clarity.

to perform a fit using the information from the full spectral window (about half the  $K$  band). In order to perform such a fit, we use the geometrical model described in Eq. 1, together with the synthetic spectra described in Sect. 3.2 (Martins et al. 2005). We are particularly interested in seeing a change in the interferometric signal associated with the predicted change of the O to WR flux ratio as we progress from continuum to line regions.

The set of observables considered to perform the fit has been extended to the full dataset, namely the spectrum, the averaged absolute visibilities and closure phase per spectral window, the differential visibilities and the differential phases.

We use non-linear fit methods in order to minimise the  $\chi^2$  between the observables and the model. Then we compute the best fit of about a thousand randomly chosen initial parameters in order to get the best minimum of  $\chi^2$ . The final model has then been compared to the observed star spectrum and interferometric observables as shown in the Fig. 5.

The best fit yields a binary star separation of  $3.64^{+0.09}_{-0.40}$  mas, a position angle of  $72^{+17}_{-14}$ °, a flux ratio of  $0.75^{+0.10}_{-0.08}$  (in the whole 1.95–2.17  $\mu\text{m}$  range), attributed here to the WR to O flux ratio. This detection is made possible because of the non-zero closure phase signal and is clearly made because of the presence of different lines in the WR- and O-star spectra.

The AMBER instrument would normally allow to disentangle definitely which component is the North-East and which is the South-West. However, the calibration data obtained for this has been taken and is still in the process of being interpreted. This is why we guess, according to a preliminary study of this calibration data, that the North-East component is the WR star and the South-West is the O star, but we are quite prudent about this particular point.

#### 4.2.2. Interpretation

We tested the fits with the full library of spectrum provided by Martins et al. (2005). The quality of the fits is only slightly affected by the choice of the O star spectrum. In the near-IR, the spectrum is weakly sensitive to the star temperature and equally good fits can be obtained with models with  $T_{\text{eff}}$  between 27kK and 35kK (or yet higher). Yet, the four spectra providing the best fits are those with  $\log g$  between 3.2 and 3.35, considering the O star as a supergiant. This information has to be taken with caution since the residuals depend critically on the choice of the WR star spectrum, but this result still holds when we consider our different WR models.

The spectrum, the differential visibilities, differential phases and closure phases are reasonably well fitted. The absolute visibilities are overestimated in our model compared to that of AMBER. Again, these discrepancies may be due to biases in the absolute visibilities of AMBER, but we note also significant departures in the differential vis-

ibilities, differential phases and closure phase at 2.08  $\mu\text{m}$  (CIV line), 2.115  $\mu\text{m}$  (CIII line) and 2.14  $\mu\text{m}$  (see Fig. 5).

As mentioned in the previous section, the simplest way to solve the absolute visibilities discrepancies is to add a fully resolved “continuum” contribution. However, the constraints provided by the differential observable and the closure phase are also tight, due to the large flux ratio variations in the WR lines. This leave only small room to even a small diluting factor. We tried to inject a fully resolved component with varying flux contribution and the maximum possible continuum contribution has been estimated to 5% of the overall flux. Within this range, the fits of the differential observables and the closure phase are slightly improved, but the discrepancies of the absolute visibilities remain.

The most convincing signature of the WWCZ may be found in lines, but in the stage of development of the WR spectrum model, it is not absolutely sure that the residuals of the fits in the lines come from an inadequacy of the models or an intrinsic signal from an additional component.

### 4.3. WR spectrum reconstruction

#### 4.3.1. Method and results

In this section, we consider that the O star spectrum is better constrained than the WR star spectrum. It is just an almost featureless continuum with a relatively well-defined slope. Hence, we try another approach based on our simple geometrical model of a binary with unresolved components of Eq. 1. Previously, the wavelength-dependent flux ratio between the O star and the WR star was defined by the ratio of the synthetic spectra.

Now, we determine for each spectral channel the WR star flux using only the observed flux and the O star model. The idea is to use all the information contained in the data in order to minimize the *a priori* information used in the model. We point out to the reader that the observed spectrum is normalized as described in Appendix B, the absolute flux information being lost.

Let  $S^{\text{GV}}(\lambda)$  be the observed spectrum,  $R$  the flux ratio between the O star and the WR star, and  $S_N^O(\lambda)$  the normalized O spectrum. We can define a normalized WR star spectrum by:

$$S_N^{\text{WR}}(\lambda) = \frac{(1 + R) * S^{\text{GV}}(\lambda) - S_N^O(\lambda)}{R} \quad (2)$$

Since the observed spectrum is normalized as described in Appendix B, we need to normalize in the same way the O star synthetic spectrum before subtracting it from the observed spectrum in order to get this normalized WR star spectrum. Then we multiply the resulting spectrum with the slope of a blackbody at 56000 K, the expected temperature of the WR star. We tested several black body temperatures such as 70000 K for example and found that it does not change dramatically the slope of the WR spectrum nor the result of the fit. This suggests that using a

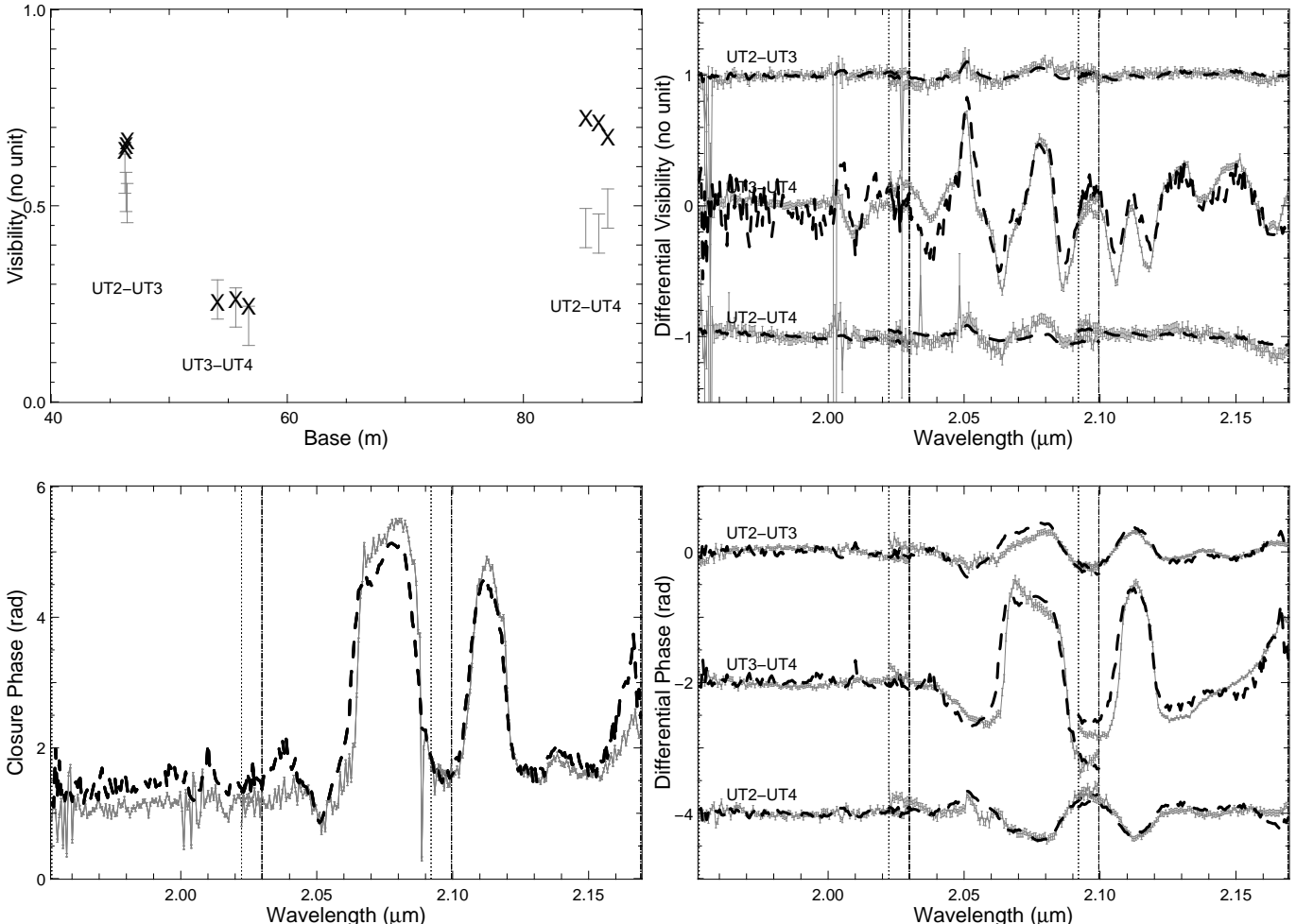


**Fig. 6.** Observed data with AMBER and the best fit, using a geometrical model of a double star, a O-star synthetic spectrum and a reconstructed WR-star spectrum of Sect. 4.3. *top-left*: Points with error bars: observed absolute visibilities versus base length. Crosses: our model. See text for comments. *top-right*: Gray line with error bars: observed differential visibilities versus wavelength. Dashed line: our model. The different baselines are offseted for clarity. *bottom-left*: Gray line with error bars: observed closure phase versus wavelength. Dashed line: the model. See text for comments. *bottom-right*: Gray line with error bars: observed differential phases versus wavelength. Dashed line: our model. The different baselines are offseted for clarity.

Black Body for this fit is approximate but adequate since the slope of the energy distribution of a WR star is not too sensitive to the temperature of the model in the 1.95–2.17  $\mu\text{m}$  range.

At this point we get a completely constrained spectrum of the WR star, only dependent from the O star model and the AMBER spectrum. We inject then the spectrum of the modeled O star and the constrained WR star in the interferometric data in order to compute a  $\chi^2$  and perform the fit.

This technique has been used to fit the data shown in Fig. 6. Compared to the previous method involving the synthetic WR spectrum, the residuals (i.e. the  $\chi^2$ ) are smaller. For instance, the contribution from the missing line at 2.138  $\mu\text{m}$ , not predicted by our WR model, is well reproduced and the residuals are small. The poor photometric quality of the spectral window between 1.95 and 2.2  $\mu\text{m}$  (and in particular the 2.01  $\mu\text{m}$  atmospheric fea-

ture) is reported in the differential visibilities (mostly the UT3-UT4 ones) and the closure phase.

This method provides the best fit to the data of the present paper and all the following is based on the results of this fit. It yields the following parameters: a binary separation of  $3.62^{+0.11}_{-0.30}$  mas, a position angle of  $73^{+9}_{-11}$   $^\circ$ , a WR flux contribution in the 1.95–2.17  $\mu\text{m}$  spectral window of  $0.79^{+0.06}_{-0.12}$ .

The parameters are basically unchanged compared to those of the previous section, suggesting that the quality of the WR synthetic spectrum does not introduce a sizable bias on our determination.

## 5. Discussion

### 5.1. Spectra separation and stars parameters

One very interesting point of the methods described above is the fact that we are able to extract a WR spectrum inde-

pendent from previous spectrophotometric measurements. This allows us to compare our best spectrum model from the fit of the Sect. 4.2 and this independently extracted spectrum. One can find the resulting spectra on the Fig. 7.

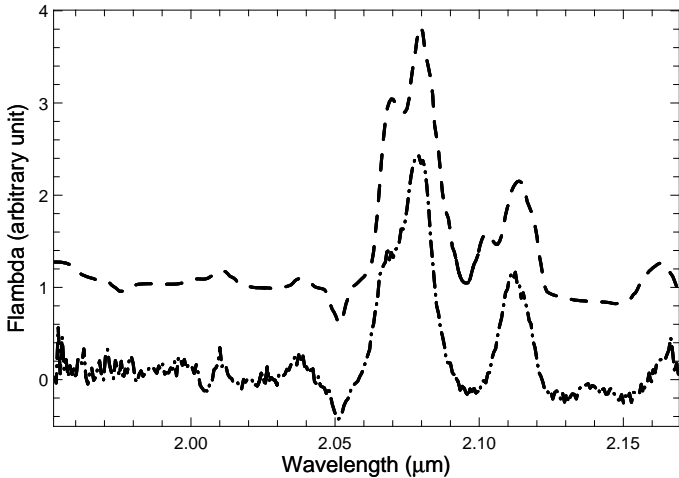


**Fig. 7.** The two final WR spectra showed on the same plot. Dashed line: WR model of Sect. 4.2. Dash-dotted line: WR spectrum of Sect. 4.3. They show similarities in the lines at  $2.059\mu\text{m}$  and  $2.165\mu\text{m}$  but our modeled spectrum is less accurate in the carbon lines at  $2.071\mu\text{m}$ ,  $2.079\mu\text{m}$ ,  $2.108\mu\text{m}$  and  $2.114\mu\text{m}$ .

## 5.2. Binary separation and distance

The geometrical parameters provided by the different approaches used to invert the data have been markedly consistent and robust. The best fit (i.e. minimum  $\chi^2$ ) and narrower error bars are found for the method in Sect. 4.3 which the WR spectrum is considered as undefined. This could appear artificial but the resemblance of the spectrum and fits estimated with the ones found using a radiative model lead us to be confident on the results presented. The parameters are shown in table 5 and the results from Sect. 4.3 are reported in Fig. 8. With this direct observation of the  $\gamma^2$  Velorum with the interferometer and our model fitting, we should be able to disentangle the  $\pi$  uncertainty between the WR and O position, the first being the North-East and the second being the South-West at the time of the observations (see the Sect. 4.2 for more details). However, this preliminary result has to be confirmed with the complete analysis of our AMBER calibration data.

The binary parameters remain unchanged within the error bars shown in the figure and do not change the present reasoning. The estimated errors on the position angle are relatively large, but comparable to the uncertainties of the spectroscopic orbit. The values agree well, which means that the projected position of the two stars is well predicted if the spectroscopic information is complemented by the polarization data from St.-Louis et al. (1987). By contrast, our estimated projected separation

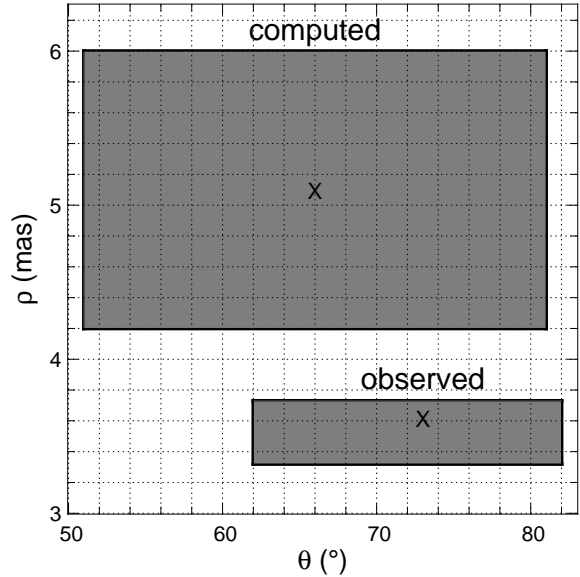


**Fig. 8.** Errors derived from the different techniques used to retrieve the geometrical parameters of the binary star at the time of the AMBER observations. The big gray box represents the estimation and error bars from the radial velocity method and the small gray box is the resulting parameters from our interferometric fit. This figure show that the direct measured separation by interferometric means is smaller than the expected one, leading to a possible reevaluation of the distance of the system.

**Table 5.** Summary of all the methods and results used in this paper, showing the good agreement we have with several different interpretation methods of the interferometric data, but the bad agreement on the separation between the interferometric methods and the spectrophotometric method.

Method	Separation (mas)	Pos. angle (°)	Averaged fx. rat. ( $1.95\text{-}2.17\mu\text{m}$ )
Sect. 3.1	$5.3^{+0.9}$	$66^{+15}$	-
Sect. 4.1	$3.65^{+0.12}$	$73^{+13}$	$0.79^{+0.12}$
Sect. 4.2	$3.64^{+0.09}_{-0.40}$	$72^{+17}_{-14}$	$0.75^{+0.10}_{-0.08}$
Sect. 4.3	$3.62^{+0.11}_{-0.30}$	$73^{+9}_{-11}$	$0.79^{+0.06}_{-0.12}$

is well-constrained and differs significantly from the predicted one. The AMBER separation is at a  $2\sigma$  level from the predicted one.

Furthermore, from the AMBER point-of-view, the spectroscopic-based separation at  $1\sigma$  in Fig. 8 is still separated to more than  $3\sigma$  of the AMBER error bar. The spectroscopic-based error bar on the separation  $\rho$  is mostly defined by the Hipparcos uncertainties. A computation of the distance including the AMBER separation and angle measurements in the frame of the spectroscopic orbit parameters leads to a distance of  $368^{+38}_{-13}$  pc.

Before the Hipparcos era, the common estimated distances to  $\gamma^2$  Velorum were typically of  $\sim 450$  pc

(Barlow et al. 1988; Stevens et al. 1996). The present estimate, with a variance at the  $2\sigma$  level from the Hipparcos measurement, would place  $\gamma^2$  Velorum within the Vela OB2 association, affecting all distance dependent parameters such as the luminosity, radii, and of course spectral types. As an example, the Table 2 reporting the parameters of De Marco et al. (2000) are scaled to the Hipparcos distance. In pre-Hipparcos area, the spectral type of the O star has been for a long time O9I (Van der Hucht et al. 1997), which means that the typical radius is about  $20R_\odot$ , rather than  $13R_\odot$ .

The reliability of the Hipparcos distance has recently been questioned by the discovery of an association of low-mass, pre-main sequence stars in the direction of  $\gamma^2$  Velorum which would have affected the measured parallax, and the distance to  $\gamma^2$  Velorum may be between 360 and 490 pc (Pozzo et al. 2000). A low-mass companion  $4.8''$  away has been observed in the X-ray band with Chandra (Skinner et al. 2001). A similar problem concerning the star WR 47 (WN6+O5V) has been reported and extensively studied by Pietti et al. which lead to a distance multiplied by 4 compared to the Hipparcos one ( $1.10 \pm 0.05$  kpc versus  $216^{+166}_{-65}$  pc<sup>4</sup>).

### 5.2.1. Residuals of the fits

In Sect. 3.2, we have documented the properties of the  $\gamma^2$  Velorum system used to estimate the observed signal with the AMBER instrument. Our interpretation suggests a binary system whose separation is resolved by the interferometer, but not their individual components diameter. Note that we have neglected the presence of dust or any other source of emission.

Different modeling methods were used, with different assumptions on the two sources, but lead to results in agreement for the binary separation, the position angle, and flux ratio between the two stars. However, in both methods, the quality of the fits could be improved. Errors and biases of the different AMBER observables may corrupt the fitting process, but the disagreements may also stem from additional components not yet accounted for.

Let us assess the source of the residuals and try to provide some information on the way the present model of the  $\gamma^2$  Velorum system could be improved. The residuals of the fits are analyzed per observable:

- Differential visibilities: The fits based on the extracted WR spectrum are of good quality and the residuals can not be attributed definitely to an additional astronomical signal. The levels of the dips and peaks of the signal are tightly correlated to the changing of the primary versus the secondary source of flux. A small change of the flux ratio between the two stars, and the inclusion of a small source of continuum can affect drastically this observable. More complex models,

<sup>4</sup> This distance would have made WR 47 the closest WR, before  $\gamma^2$  Velorum.

e.g., including a continuum contribution of up to 5% of the total flux, improve slightly the match with the observations.

- Differential phases: the quality of the fits is reasonably good considering that this observable is subject to continuum fluctuations that can be seen, for instance, in the edge of the spectral window at  $2.17\mu\text{m}$ . We note a discrepancy of the model and the signal at  $2.07\mu\text{m}$  for the baselines UT2-UT3 and UT3-UT4. This discrepancy is only slightly attenuated when using the WR synthetic spectrum that shows a stronger contribution at this wavelength than observed. This may indicate an additional source of emission for this particular line at a position not coincident with that of the WR star. The balance of the different contributions of these blended lines is temperature dependent and the WWCZ can add both a spatial and a spectral signature.
- Closure phase: there is a noticeable departure of the model in the  $1.95\text{--}2.03\mu\text{m}$  spectral window. The lines are not fitted perfectly but the residuals are at the 10% level. This may suggest a third source in the system, but as before there is an ambiguity in the interpretation of this observable and a slight change in the shape of the WR lines and/or in the star-flux ratio could also change this inferred closure phase.
- Absolute visibilities: whatever the strategy used to fit the AMBER data, the model fails to provide the low level of absolute visibilities observed. The obvious solution is the introduction of a third source of continuum flux. However the contribution from an additional source is strongly limited by the other observables, requiring that the modulation of the signal by the WR is sufficient to explain the level of spectral variations observed. We tested some models with a small amount of (flat) continuum that improved slightly the model level but insufficiently. For this observable though, we think that some instrumental effect on UT2 biased the visibilities.

At this stage of the analysis and given the limited amount of data available, it is not possible to attribute with confidence the residuals to an astrophysical origin. However, we have several observables that have significant discrepancies in some lines, giving tenuous clues that something more has to be included in our model to improve the fits. More data is needed, covering a broad range of binary phases, in order to get more constraints on a complete model.

## 6. Conclusion

Using a relatively restrained data set from the AMBER/VLTI instrument, we have set tight constraints on the geometrical parameters of the  $\gamma^2$  Velorum orbit. This separation leads to a reevaluation of the distance of the  $\gamma^2$  Velorum system that has to be confirmed and more accurately estimated by a regular monitoring of the system.

Moreover, we were able to perform a spectrum separation between the two stars, using known assumptions on the spectral type of the O star. This allowed us to compare our modeled WR spectrum to this independent one and found that their match is reasonable.

We note however that the observed data set is not fully consistent with a simple geometrical binary model taking into account refinements of the modeled spectra for each component. This discrepancy may be interpreted as not well understood instrumental biases as well as the detection of a spatially distinct source of continuum, that would contribute to up to 5% of the total flux of the system.

*Acknowledgements.* We warmly thank John Davis and Julian North for fruitful discussions on the definition of polarimetric versus spectroscopic parameters of binary orbits that allowed us to detect an inconsistency on the direction of the orbit in the paper.

We thank Fabrice Martins for providing the O star synthetic spectrum. This paper makes use of *Jean-Marie Mariotti Center* (JMMC) tools for model fitting and data adjustment.

We would like to thank the staff of the European Southern Observatory for their help in the design and the commissioning of the AMBER instrument.

This project has benefited from funding from the French Centre National de la Recherche Scientifique (CNRS) through the Institut National des Sciences de l'Univers (INSU) and its Programmes Nationaux (ASHRA, PNPS). The authors from the French laboratories would like to thank the successive directors of the INSU/CNRS directors. The authors from the Arcetri Observatory acknowledge partial support from MIUR grants and from INAF grants. C. Gil work was supported in part by the Fundação para a Ciência e a Tecnologia through project POCTI/CTE-AST/55691/2004 from POCTI, with funds from the European program FEDER.

This research has also made use of the ASPRO observation preparation tool from the JMMC in France, the SIMBAD database at CDS, Strasbourg (France) and the Smithsonian/NASA Astrophysics Data System (ADS). This publication makes use of data products from the Two Micron All Sky Survey.

The AMBER data reduction software `amplib` has been linked with the open source software Yorick<sup>5</sup> to provide the user friendly interface `ammyorick`. They are freely available on the AMBER website <http://amber.obs.ujf-grenoble.fr>.

## References

Barlow, M. J., Roche, P. F., & Aitken, D. K. 1988, MNRAS, 232, 821

Brown, J. C., Aspin, C., Simmons, J. F. L., & McLean, I. S. 1982, MNRAS, 198, 787

Corcoran, M. F., Hamaguchi, K., Henley, D., et al. 2003, American Astronomical Society Meeting Abstracts, 203

De Marco, O. & Schmutz, W. 1999, A&A, 345, 163

De Marco, O., Schmutz, W., Crowther, P. A., et al. 2000, A&A, 358, 187

Dessart, L., Crowther, P. A., Hillier, D. J., et al. 2000, MNRAS, 315, 407

Hanbury Brown, R., Davis, J., Herbison-Evans, D., & Allen, L. R. 1970, MNRAS, 148, 103

Hanson, M. M., Conti, P. S., & Rieke, M. J. 1996, ApJS, 107, 281

Henley, D. B., Stevens, I. R., & Pittard, J. M. 2005, MNRAS, 356, 1308

Hillier, D. J. & Miller, D. L. 1998, ApJ, 496, 407

Malbet, F., Benisty, M., De Wit, W. J., et al. 2005, A&A, -, In Press

Martins, F., Schaefer, D., & Hillier, D. J. 2005, A&A, 436, 1049

Mege, P., Malbet, F., & Chelli, A. 2000, in Proc. SPIE Vol. 4006, p. 299-307, Interferometry in Optical Astronomy, Pierre J. Lena; Andreas Quirrenbach; Eds., ed. P. J. Lena & A. Quirrenbach, 299–307

Millour, F., Tatulli, E., Chelli, A. E., et al. 2004, in New Frontiers in Stellar Interferometry., ed. W. A. Traub, Vol. 5491 (SPIE), 1222

Millour, F., Vannier, M., Petrov, R. G., et al. 2006, in Astronomy with High Contrast Imaging III: Instrumentation and data processing, ed. C. Aime, A. Ferrari, & M. Carillet (EAS Publications Series), in press

Monnier, J. D., Greenhill, L. J., Tuthill, P. G., & Danchi, W. C. 2002, in ASP Conf. Ser. 260: Interacting Winds from Massive Stars, ed. A. F. J. Moffat & N. St-Louis, 331

Perrin, G. 2003, A&A, 400, 1173

Petrov, R. G., Malbet, F., Weigelt, G., et al. 2003, in Interferometry for Optical Astronomy II. Edited by Wesley A. Traub . Proceedings of the SPIE, Volume 4838, pp. 924-933 (2003)., ed. W. A. Traub, 924–933

Pittard, J. M. & Stevens, I. R. 2002, A&A, 388, L20

Pozzo, M., Jeffries, R. D., Naylor, T., et al. 2000, MNRAS, 313, L23

Schaefer, D., Schmutz, W., & Grenon, M. 1997, ApJL, 484, L153

Schild, H., Güdel, M., Mewe, R., et al. 2004, A&A, 422, 177

Schmutz, W., Schweickhardt, J., Stahl, O., et al. 1997, A&A, 328, 219

Skinner, S. L., Güdel, M., Schmutz, W., & Stevens, I. R. 2001, ApJL, 558, L113

St.-Louis, N., Drissen, L., Moffat, A. F. J., Bastien, P., & Tapia, S. 1987, ApJ, 322, 870

St.-Louis, N., Willis, A. J., & Stevens, I. R. 1993, ApJ, 415, 298

Stevens, I. R., Corcoran, M. F., Willis, A. J., et al. 1996, MNRAS, 283, 589

Tatulli, E., Millour, F., Chelli, A., et al. 2006, A&A, -, In Press

Van der Hucht, K. A. 2002, ApSS, 281, 199

Van der Hucht, K. A., Morris, P. W., Williams, P. M., et al. 1996, A&A, 315, L193

Van der Hucht, K. A., Schrijver, H., Stenholm, B., et al. 1997, New Astronomy, 2, 245

Villar-Sbaffi, A., St-Louis, N., Moffat, A. F. J., & Piirola, V. 2005, ApJ, 623, 1092

<sup>5</sup> <http://yorick.sourceforge.net>

Willis, A. J., Schild, H., & Stevens, I. R. 1995, A&A, 298, 549

## Appendix A: Data processing status

AMBER follows the standard data flow system implemented at ESO/VLT. During data acquisition, the software records the images of the spectrally dispersed fringes as well as those of the telescope beams.

The standard data reduction method developed and optimized for AMBER is called P2VM for Pixel-To-Visibilities Matrix (Tatulli et al. 2006; Millour et al. 2004). The P2VM is a linear matrix method which computed raw visibilities from AMBER data for each spectral channel. The P2VM is computed after an internal calibration procedure which is performed every time the instrument configuration changes. The complex coherent fluxes are given by the product of the fluxes measured on each pixel of the detector by this P2VM matrix. We then compute all the useful observables, namely the visibility, the closure phase, the differential visibility, and the differential phase. For more details, please refer to Tatulli et al. (2006); Millour et al. (2004).

## Appendix B: Spectral calibration

The atmosphere imprints its signature on the observed spectrum of  $\gamma^2$  Velorum, namely through the characteristic CO<sub>2</sub> rovibrationnal lines at 2.01  $\mu\text{m}$  and 2.06  $\mu\text{m}$ . Using a reference spectrum of the atmospheric transmission and correlation techniques, we get an absolute and accurate (half a pixel, to be compared to the 2 pixels sampling of the spectrum) spectral calibration of the observed spectrum (see Fig. A.1)

We corrected the spectra for telluric lines by observing the calibration star approximately at the same airmass and dividing the two spectra (the same technique as Hanson et al. (1996)).

As we observed at medium spectral resolution ( $R \sim 1500$ ), the numerous narrow spectral features in the A star spectrum are smeared out, with the exception of  $B\gamma\gamma$ . The calibrator spectrum is therefore featureless and allows a good correction of the telluric lines. The  $B\gamma\gamma$  line at 2.165  $\mu\text{m}$  is removed from the calibrator spectrum by fitting a Voigt profile (see the left panel of Fig. A.1).

No accurate correction from the telluric spectrum is performed in the area of the  $B\gamma\gamma$  line due to the narrowness of the spectral window that lack strong telluric lines. The airmass was 1.2 for  $\gamma^2$  Velorum and 1.1 for the calibrator star which leads to an error on the calibrated spectrum of about 7% in the parts where there is strong atmosphere absorption lines (e.g. around 2.00  $\mu\text{m}$ ). This systematic error is taken into account in the calibrated spectrum error bars.

AMBER collects the stellar fluxes through optical fibers. Taking into account the rapidly varying tip/tilt

effect on the fiber entrance, the changes in airmass, seeing conditions, and vibrations conditions between the star and calibrator, it is not possible to extract a reliable absolute flux from the observed star. The observed spectrum is continuum corrected by means of a spline curve that passes through designated continuum regions. This yields a totally flat observed spectrum as in the top panel of Fig. 2. The error bars of the resulting spectrum takes into account the detector noise and the photon noise, as well as the air mass mismatch between the calibrator and the science stars.

## Appendix C: Data selection and biases

The specific conditions of observations described above make the selection of the data sample difficult. The data reduction technique provides accurate results when the sub-set of good frames selected for the science and calibration object are unbiased. In our case, the science and calibration stars have only one magnitude difference and the average seeing was 0.65'' for  $\gamma^2$  Velorum and 0.7'' for the calibration star.

To select the data, we compute all the observables and then estimate the biases introduced on the absolute visibilities by comparing different frame selection thresholds (see Fig. A.1). The selection criterion is set by a threshold value of the coherent flux signal-to-noise ratio (SNR) for individual frames. We obtain a constant value of visibility whatever the threshold, which suggests that the frame selection criterion does not bias the estimated  $\gamma^2$  Velorum absolute visibilities in the range of the estimated error bars.

We based our optimum SNR threshold selection on the minimum of the statistical errors computed on the absolute visibilities. This optimum threshold keeps 20% of the total number of frames (Fig. A.1, left panel).

## Appendix D: Observables calibration

We calibrate the absolute visibilities using the technique described in Perrin (2003): we interpolate the calibrator visibilities at the time of the science star observations in order to correct it from the instrumental and atmospheric transfer functions. The calibrator visibilities are corrected from the resolved flux level based on its estimated angular diameter.

$$V^{\text{GV}} = 2 \frac{J_1\left(\frac{\pi B \theta}{\lambda}\right)}{\frac{\pi B \theta}{\lambda}} \frac{V_{\text{raw}}^{\text{GV}}}{V^{\text{cal}}}, \quad (\text{D.1})$$

where  $B$  is the base length,  $\theta_{\text{cal}}$  the estimated diameter of the calibrator star,  $V_{\text{raw}}^{\text{GV}}$  being the raw visibilities of  $\gamma^2$  Velorum, and  $V^{\text{cal}}$  the visibility of the calibrator star interpolated to the observation time.

For the closure phase, we only correct the object closure phase from any instrumental-based signal by subtracting the calibrator closure phase and the object closure phase,

$$\psi_{\text{diff}}^{\text{GV}} = \psi_{\text{diff raw}}^{\text{GV}} - \psi_{\text{diff raw}}^{\text{cal}}. \quad (\text{D.2})$$

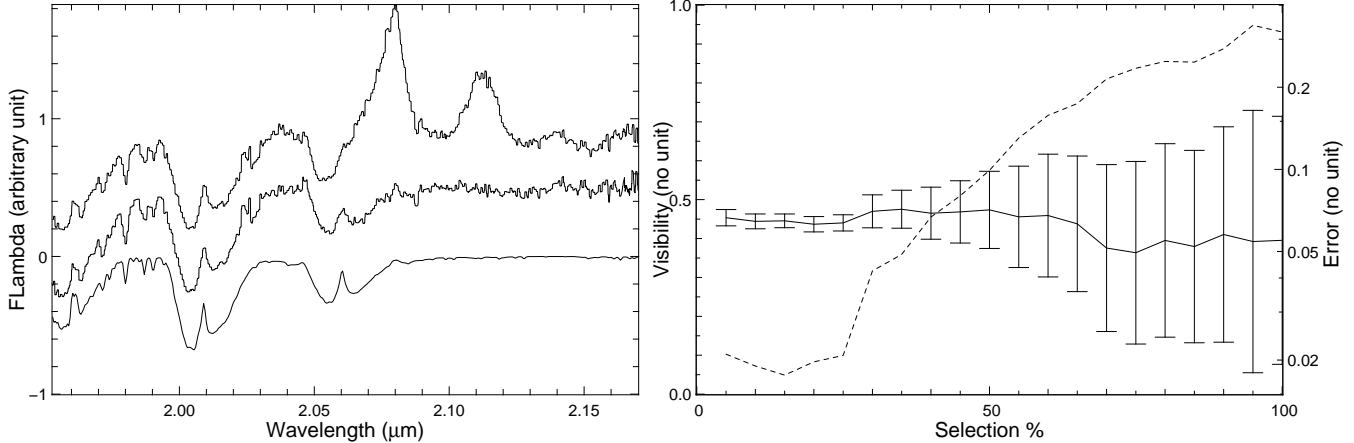


**Fig. A.1.** *Left:* Calibration of the spectral drift, using the reference star spectrum (flat A1III star spectrum). From top to bottom are the uncalibrated observed  $\gamma^2$  Velorum spectrum, the calibrator star spectrum after removal of a Voigt profile in the  $\text{Br}\gamma$  line, and the reference Gemini spectrum. All of them show a clear  $\text{CO}_2$  rovibrational feature at  $2.01\mu\text{m}$  and  $2.06\mu\text{m}$ , and some other water vapor absorption lines, used for the absolute wavelength calibration. The graphs have been offset for clarity. *Right:* Estimate of the absolute visibilities by applying different frame selection thresholds keeping percentage of the observed frames (solid line with error bars, left axis). The internal dispersion of the visibilities increases as the amount of data rejected decreases but there is no obvious bias coming from data selection as the absolute visibilities stays constant within the error bars. The optimal selection threshold is chosen at the position of minimum of the statistical dispersion of the squared visibilities (dashed line, right axis): in this data set, this level keeps 20% of the observed frames (i.e. 80% rejected).

The differential visibilities and differential phase are computed as explained in Millour et al. (2006), and should need no calibration, at least in theory. However, we noticed that they are affected by instrumental effects such as polarization mismatch between the fibers outputs, leading to differential phase effects up to 0.05 rad peak to peak.

For the differential visibility, the calibration is performed by dividing the star by the calibrator differential visibilities:

$$V_{\text{diff}}^{\text{GV}} = \frac{V_{\text{diff raw}}^{\text{GV}}}{V_{\text{diff raw}}^{\text{cal}}} \quad (\text{D.3})$$

For the differential phase, the calibration is performed by subtracting the calibrator to the star differential phase:

$$\phi_{\text{diff}}^{\text{GV}} = \phi_{\text{diff raw}}^{\text{GV}} - \phi_{\text{diff raw}}^{\text{cal}} \quad (\text{D.4})$$

## Appendix E: Error Estimates

The statistical errors are estimated using the dispersion of the individual-frame observables, assuming a Gaussian distribution of differential visibilities, differential phases and closure phase.

The limitations of the VLTI + AMBER instrument described in Appendix A (vibrations, large amount of time between the star and calibrator) and the level of dispersion of the absolute visibilities observed with other calibrators (in different spectral band) led us to increase the estimated error bars beyond the natural dispersion of the absolute visibilities. We found that the errors between calibrators are typically 5% above the internal dispersion, and, thus,

this error has been added to the error budget. Hence, the absolute visibility error bars contain two contributions: the statistical dispersion of the measured spectrally dispersed absolute visibilities and the bias error of the mean visibilities in a spectral window, estimated to be 5%.

<sup>1</sup> Laboratoire Universitaire d'Astrophysique de Nice, UMR 6525 Université de Nice/CNRS, Parc Valrose, F-06108 Nice cedex 2, France

<sup>2</sup> Laboratoire d'Astrophysique de Grenoble, U.M.R. 5571 Université Joseph Fourier/C.N.R.S., BP 53, F-38041 Grenoble Cedex 9, France

<sup>3</sup> Laboratoire Gemini, U.M.R. 6203 Observatoire de la Côte d'Azur/C.N.R.S., Avenue Copernic, 06130 Grasse, France

<sup>4</sup> INAF-Osservatorio Astrofisico di Arcetri, Istituto Nazionale di Astrofisica, Largo E. Fermi 5, I-50125 Firenze, Italy

<sup>5</sup> Max-Planck-Institut für Radioastronomie, Auf dem Hügel 69, D-53121 Bonn, Germany

<sup>6</sup> Steward Observatory, University of Arizona, 933 North Cherry Avenue, Tucson, AZ 85721, USA

<sup>7</sup> Centre de Recherche Astronomique de Lyon, U.M.R. 5574 Université Claude Bernard/C.N.R.S., 9 avenue Charles André, F-69561 Saint Genis Laval cedex, France

<sup>8</sup> European Southern Observatory, Casilla 19001, Santiago 19, Chile

<sup>9</sup> European Southern Observatory, Karl Schwarzschild Strasse 2, D-85748 Garching, Germany

<sup>10</sup> IRCOM, U.M.R. 6615 Université de Limoges/C.N.R.S., 123 avenue Albert Thomas, F-87060 Limoges cedex, France

<sup>11</sup> Division Technique INSU/C.N.R.S. UPS 855, 1 place Aristide Briand, F-92195 Meudon cedex, France

<sup>12</sup> ONERA/DOTA, 29 av de la Division Leclerc, BP 72, F-92322 Châtillon Cedex, France

<sup>13</sup> Instituut voor Sterrenkunde, KULeuven, Celestijnenlaan  
200B, B-3001 Leuven, Belgium

<sup>14</sup> *Present affiliation:* Laboratoire Astrophysique de Toulouse,  
UMR 5572 Université Paul Sabatier/CNRS, BP 826, F-  
65008 Tarbes cedex, France

<sup>15</sup> *Present affiliation:* Observatoire de la Côte d'Azur - Caïren,  
2130 Route de l'Observatoire, F-06460 Caussols, France

